ACS OMEGA

http://pubs.acs.org/journal/acsodf

Article

Nd−Nb Co-doped SnO_2/α-WO_3 Electrochromic Materials: Enhanced Stability and Switching Properties

Ronn Goei,* Amanda Jiamin Ong, Jun Hao Tan, Jie Yi Loke, Shun Kuang Lua, Daniel Mandler, Shlomo Magdassi, and Alfred Iing Yoong Tok*

Cite This: *ACS Omega* 2021, 6, 26251−26261

Read Online

ACCESS | Metrics & More | Article Recommendations

ABSTRACT: The fabrication of Nd−Nb co-doped SnO_2/α-WO_3 electrochromic (EC) materials for smart window applications is presented in the present paper. Nb is a good dopant candidate for ECs owing to its ability to introduce active sites on the surface of α-WO_3 without causing much lattice strain due to the similar ionic radius of Nb^{5+} and W^{6+}. These active sites introduce more channels for charge insertion or removal during redox reactions, improving the overall EC performance. However, Nb suffers from prolonged utilization due to the Li^+ ions trapped within the ECs. By coupling Nd with Nb, the co-dopants would transfer their excess electrons to SnO_2, improving the electronic conductivity and easing the insertion and extraction of Li^+ cations from the ECs. The enhanced Nd−Nb co-doped SnO_2/α-WO_3 exhibited excellent visible light transmission (90% transmittance), high near-infrared (NIR) contrast (60% NIR modulation), rapid switching time (~1 s), and excellent stability (>65% of NIR modulation was retained after repeated electrochemical cycles). The mechanism of enhanced EC performance was also investigated. The novel combination of Nd−Nb co-doped SnO_2/α-WO_3 presented in this work demonstrates an excellent candidate material for smart window applications to be used in green buildings.

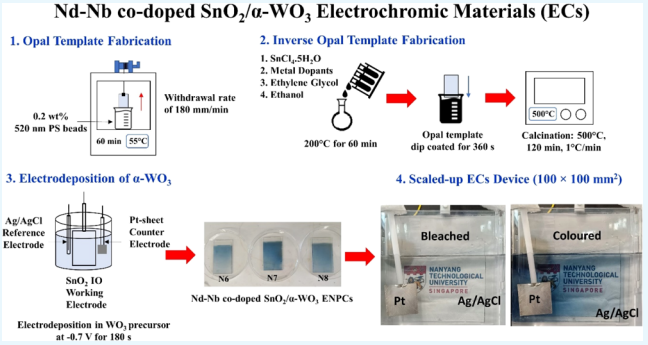

1. INTRODUCTION

Approximately 30−40% of electrical energy consumption in residential and commercial buildings is spent on lighting and thermal management system. The amount of electrical energy demand is even intensified in urbanized cities. For example, Singapore (population density of approximately 8000 per km^2), in 2019, consumed 51.7 TWh of electrical energy, of which 17.5 TWh (~34%) was used for lighting and indoor cooling.[1,2] Majority of this electrical energy (around 80%) was generated from fossil fuels.[3] The generation of electrical energy from fossil fuels emits large amounts of carbon dioxide, CO_2—a major component of greenhouse gases−−to the atmosphere. Reducing the electrical energy consumption is a prerequisite for a newer and greener smart building design.

The utilization of smart windows in commercial and residential buildings promises a more sustainable consumption of electrical energy through the ability to control cross-sectional heat modulation without compromising its visible light transparency.[4,5] In this way, one can minimize the electrical consumption inside a building from lighting and air conditioning simultaneously. Electrochromic (EC) materials were first investigated by Platt in 1961.[6] The spectro-optical properties of the ECs can be easily modified through the application of small electrical charge, making them suitable candidate materials for smart windows.[5,7−9] ECs may exist as organic, inorganic, or hybrid materials.[5,10−13] A good EC for smart window applications should possess the following properties: excellent coloration efficiency (CE), rapid tunable light and energy transmittance, good long-term stability, and good aesthetics.[8] The dual-band modulation, the ability to simultaneously tune near-infrared (NIR) irradiation and visible light transmission, is a very important characteristic of smart window materials that allow the optimization of seasonal consumption of indoor electrical energy. In this aspect, many organic ECs do not exhibit the needed dual-band modulation.[11,13,14]

On the other hand, inorganic ECs exhibited the dual-band modulation characteristics, a prerequisite for a good smart window material. Research efforts had been devoted to study iridium oxide (IrO),[15−17] molybdenum oxide (MoO_3),[18−21] nickel oxide (NiO),[22−25] niobium oxide (Nb_2O_5),[26−30]

Received: June 22, 2021
Accepted: August 10, 2021
Published: September 28, 2021

© 2021 The Authors. Published by American Chemical Society

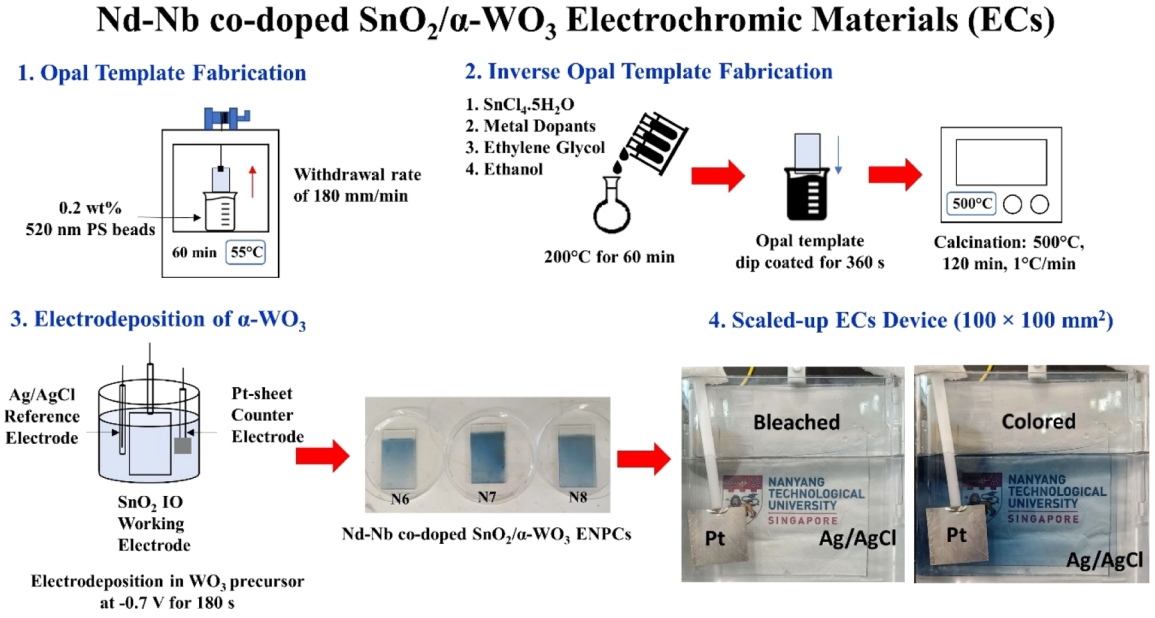

Figure 1. Fabrication of Nd−Nb co-doped SnO_2/α-WO_3 ECs.

titanium dioxide (TiO_2),[9,31−34] tungsten oxide (WO_3),[35−42] vanadium oxide (VO_2 or V_2O_5),[43−46] and their combination as suitable smart window materials. Among the abovementioned ECs, amorphous α-WO_3 is preferred due to its low cost and its excellent EC properties. The EC property of WO_3 is based on the simple principle of reversible electrochemical insertion or extraction of charge carriers and its countercations (such as H^+, Li^+, Na^+, or K^+) into/from the lattice of multivalent transition-metal ions. This reversible electrochemical reaction causes the optical modulation of α-WO_3 between the transparent and deep blue-colored state, as represented by eq 1. The three-dimensional tunnel network within the α-WO_3 octahedral framework is responsible for the ease of electron and small cation transport during the electrochemical insertion/extraction cycle, resulting in excellent EC properties.[5]

$$[W^{6+}O_3 + xM^+ + xe^-]_{\text{transparent}} \leftrightarrow [M_xW_{1-x}{}^{6+}W_x{}^{5+}O_3]_{\text{dark blue}} \quad (1)$$

Despite its excellent EC properties, α-WO_3 suffers "ion-trapping" phenomenon in which the electronic capacity of the α-WO_3 framework is reduced due to the trapped ions during the prolonged reversible electrochemical cycles.[38,47,48] The crystallization and corrosion of α-WO_3 are also responsible for the poor long-term performances of α-WO_3 ECs.[48,49] The efforts to improve the long-term performances of α-WO_3 include constant current ion de-trapping, use of templating agent, or introduction of metal dopants onto the α-WO_3 framework.[26,29,36,39,40,50−53]

The conventional WO_3 only works efficiently in the visible light range. On the other hand, by combining SnO_2 with amorphous WO_3 (SnO_2/α-WO_3), the composite can modulate infra-red (IR) and near infra-red (NIR) light, which account for nearly 50% of the thermal energy in the solar spectrum while improving the visible light transparency of the ECs. The addition of SnO_2 to WO_3 will impede the rearrangement of the WO_6 octahedra from crystallizing, thus improving the overall stability of the EC.[54,55] Effort to improve the EC stability of α-WO_3 includes the addition of dopants into α-WO_3. However, the addition of dopants into α-WO_3 limits the ion insertion capability and the resulting EC performance.[26,36,40,50] In our previous works, we have investigated different metal dopants incorporated onto a bare SnO_2/α-WO_3 framework: Nb, Mo, Ti, or Fe.[56] The addition of metal dopants was able to effect the dual-band modulation, and improved CE and fast switching time with Mo-doped SnO_2/α-WO_3 exhibited the best EC performance. We further introduced a novel concept of second metal co-dopant (a lanthanide−neodymium) onto Mo-doped SnO_2/α-WO_3 ECs.[57] We found that the introduction of Nd as a co-dopant enhanced the performances of Mo-doped SnO_2/α-WO_3 ECs which caused the improved electronic conductivity of SnO_2/α-WO_3 caused by the introduction of an energy state within the band gap of SnO_2.[40,58,59] Reichman and Bard discovered the electrochromism of Nb_2O_5 in 1980[60] which triggered an extensive study of Nb_2O_5 as EC materials. Niobium exists in various oxidation states (i.e. +2, +4, or +5), oxide polymorphic forms, and morphologies. Nb can be used as a dopant to enhance the EC performance of other EC materials, such as organic poly(ethylene-3,4-dioxythiophene)/poly(styrene sulfonic acid)[28] and inorganic metal oxides,[29,30,61] or to be used as its own EC materials.[41,62] The addition of Nb onto SnO_2/α-WO_3 will enhance the performance of SnO_2/α-WO_3 due to the introduction of defect states and provision of active sites for reactions on the surface of α-WO_3 without introducing a lattice strain on the overall structure.[61,63] We aim to demonstrate the improved EC performance through the introduction of a novel co-dopant combination of neodymium and niobium (Nd−Nb) onto the SnO_2/α-WO_3 EC framework. Nb as a sole dopant suffers from EC performance drop over a prolonged utilization. We propose that Nd−Nb will work synergistically to enhance the performance of SnO_2/α-WO_3 ECs. To the best of the authors' knowledge, this is a maiden work that investigates the synergistic introduction of Nd−Nb metal co-dopants into the SnO_2/α-WO_3 EC framework and its effect on the enhanced stability and switching properties of the ECs. This work would show an important use of SnO_2/α-WO_3 ECs as efficient, stable, and long-lasting smart window materials. The energy-saving

https://doi.org/10.1021/acsomega.1c03260
ACS Omega 2021, 6, 26251−26261

performance, lighting performance, ease of operation and control, and durability of the ECs are important prerequisites for the use of ECs for smart windows in green buildings.[64]

2. EXPERIMENTAL SECTION

2.1. Materials and Reagents. Nd−Nb co-doped SnO_2/α-WO_3 ECs were prepared using the following chemicals acquired from Sigma-Aldrich and used without any further purification: tin(IV) chloride pentahydrate ($SnCl_4{\cdot}5H_2O$), niobium(V) chloride, neodymium(V) chloride hexahydrate ($NdCl_5{\cdot}6H_2O$), ethylene glycol (EG), hydrated sodium tungstate ($Na_2WO_4{\cdot}2H_2O$), hydrogen peroxide (H_2O_2), and chloric(VII) acid ($HClO_4$). Milli-Q water (18.2 MΩ cm at 25 °C) was used for synthesis and other processes.

The Nd−Nb co-doped SnO_2/α-WO_3 ECs were constructed on a cleaned 5.0 × 3.5 cm^2 glass substrate [fluorine-doped tin oxide (FTO), Wintek Technology]. To remove impurities, the substrates were ultrasonically cleaned sequentially (for 30 min each) in acetone, methanol, ethanol, and Milli-Q water. The as-cleaned substrates were stored submerged in 50% ethanol−50% Milli-Q water mixtures.

A polystyrene (PS) sphere suspension (520 nm, Thermo Fisher Scientific) was used to prepare the opal template. Optical and EC characteristics of the resulting ECs were assessed in 1 M $LiClO_4$ in propylene carbonate (PC) electrolyte solution.

2.2. Fabrication of Nd−Nb Co-doped SnO_2/α-WO_3 ECs. Figure 1 illustrates the step-by-step construction of Nd−Nb co-doped SnO_2/α-WO_3 ECs. A regular array of PS spheres was coated using an automated dip coating machine (MTI Corporation, PTL-MMB01). A previously cleaned FTO substrate was dipped (rate of 180 mm. min^{-1}) in a 0.2 wt % PS sphere suspension and kept for 90 min at 55 °C.

Inverse opal (IO) precursors were synthesized by dissolving 2.8 g of $SnCl_4{\cdot}5H_2O$ in 40 mL of EG under continuous stirring. Varying amounts of dopant precursors ($NbCl_5$ and/or $NdCl_5{\cdot}6H_2O$) were added to prepare different precursors based on the samples listed in Table 1. The precursors were kept at 200 °C for 60 min.

Table 1. Dopant Content of the ECs Prepared

EC samples	Nb dopant (% mol Sn)	Nd Co-dopant (% mol Sn)
	Undoped sample	
N1	0	0
	Nb-Doped samples	
N2	5	0
N3	10	0
N4	15	0
	Nd-Doped Sample	
N5	0	10
	Nd−Nb-Co-doped Samples	
N6	5	10
N7	10	10
N8	15	10

The viscosity of the precursor was reduced by adding 80 mL of ethanol to the cooled solution.[65] The IO samples were prepared by dip coating the as-prepared PS opal onto the IO precursor solution (360 s, room temperature). IO samples were dried at room temperature and heat-treated at 500 °C for 120 min (heating rate of 1 °C/min) to obtain the Nd−Nb co-doped SnO_2 IO.

The α-WO_3 precursor was synthesized by dissolving 1 g of $Na_2WO_4{\cdot}2H_2O$ in 0.65 mL of H_2O_2 containing Milli-Q water solution. The acidity of the precursor was lowered to pH 1.2 using a $HClO_4$ solution.[35] Lastly, the construction of the Nd−Nb co-doped SnO_2/α-WO_3 EC structure was completed by electrodepositing the α-WO_3 precursor onto the IO samples (V = −0.7 V, 180 s, Autolab Potentiostat 1470E). The as-fabricated ECs were washed and dried overnight at room temperature.

2.3. Characterization Methodology. The surface chemistry and mineralogy of the ECs were characterized using X-ray photoelectron spectroscopy (XPS, Al Kα excitation source $h\nu$ = 1486.71 eV, Shimadzu Kratos Axis Supra) and X-ray diffraction (XRD, $\lambda_{Cu\ K\alpha}$ = 1.5406 Å, Shimadzu XRD-6000). The morphology of the ECs was observed with atomic force microscopy (AFM, Park System NX10), field emission scanning electron microscopy (FESEM, JEOL 7600F), and transmission electron microscopy (TEM, JEOL 2100F).

2.4. Evaluation of the Stability and Switching Properties of Nd−Nb Co-doped SnO_2/α-WO_3 ECs. A standard three-electrode system was used to evaluate the stability and switching properties of the resulting ECs. An Ag/AgCl electrode and 1 cm^2 platinum plate were employed as reference and counter electrodes, respectively.

Cyclic voltammetry (CV) measurements of the ECs were carried out at the scan rates of 50 mV s^{-1} at the potential range between −1.2 and +1.0 V in a 1 M $LiClO_4$/PC electrolyte solution (CH Instruments 750E). The spectroelectrochemical properties of the EC samples were studied using a tandem Autolab 1470E potentistat and a UV−vis−NIR spectrophotometer (Agilent Varian Cary 5000). The UV−vis−NIR spectra were collected at the applied bias of −0.5 and +0.8 V within the wavelength range of 300−1600 nm.

The CE value of the EC samples was calculated using eq 2, where Q is the sample charge density (C cm^{-2}) and T_c, T_b, A_c, and A_b are the transmission and absorbance values in the colored and bleached states (measured at λ = 1033 nm), respectively. The value of Q was calculated from the current profile generated from the electrochemical station normalized against the effective area where the redox reactions took place.

$$CE = \frac{\Delta OD}{Q} = \frac{\log\left(\frac{T_b}{T_c}\right)}{Q} = \frac{A_b - A_c}{Q} \quad (2)$$

The switching properties of the EC samples were evaluated based on the dynamic optical transmittance performance under the influence of the repeated application of the square wave potentials (−0.5 and +0.8 V, 100 s step size). The stability of the EC samples was also evaluated through the application of up to 1000 periodic cyclic square wave potentials. Finally, the EC performance drop (EPD)—a measure of EC stability—of the samples was established according to eq 3, where $\Delta T_{initial}$ and ΔT_{after} are the NIR contrast measured at the wavelength of 1033 nm before and after the periodic cyclic test, respectively.

$$EPD\ (\%) = \frac{\Delta T_{initial} - \Delta T_{after}}{\Delta T_{initial}} \times 100\% \quad (3)$$

https://doi.org/10.1021/acsomega.1c03260
ACS Omega 2021, 6, 26251−26261

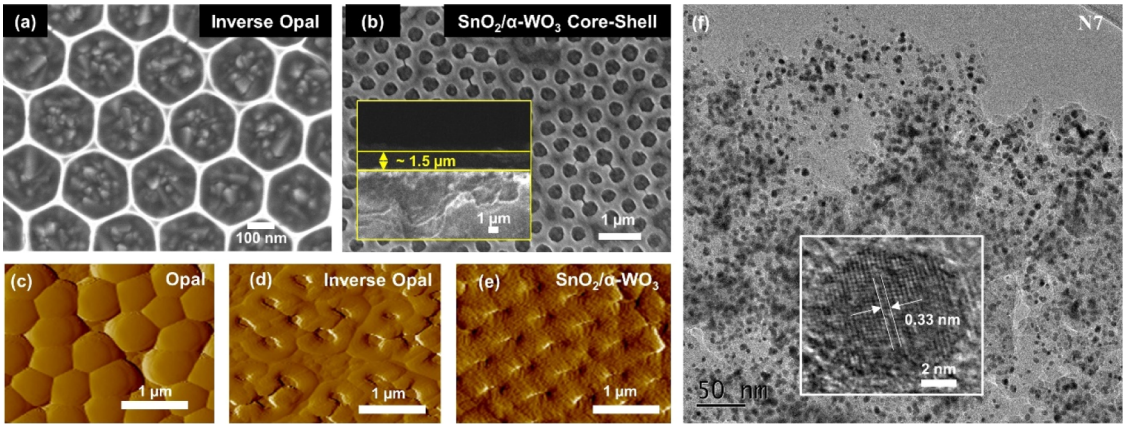

Figure 2. Morphology of the Nd−Nb co-doped SnO_2/α-WO_3 ECs networks: (a) FESEM image of the metal-doped SnO_2 structure; (b) FESEM images of the metal-doped SnO_2/α-WO_3 core−shell structure [with the inset in (b) showing the thickness of the SnO_2/α-WO_3 layer]; (c−e) AFM images of opal, inverse opal, and SnO_2/α-WO_3 layers; and (f) HRTEM images of Nd−Nb co-doped SnO_2/α-WO_3 ECs (sample N7), with the inset showing the lattice spacing of 0.33 nm which corresponds to the (110) planes of SnO_2 crystals.

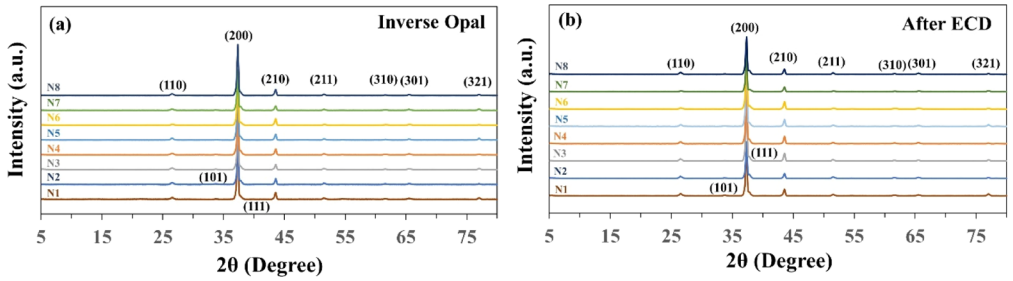

Figure 3. XRD spectra of samples N1−N8 of Nd−Nb co-doped SnO_2 (a) IO and (b) ECs after the electrochemical deposition of theα-WO_3 layer.

3. RESULTS AND DISCUSSION

3.1. Preparation and Characterization of the Nd−Nb Co-doped SnO_2/α-WO_3 ECs. Figure 1 illustrates the fabrication steps of Nd−Nb co-doped SnO_2/α-WO_3 ECs. First, the uniform opal template must be assembled from the arrays of 520 nm polystyrene (PS) spheres dip-coated onto the cleaned FTO glass. Following steps are carefully carried out during the preparation of the opal template to ensure uniform coating: (1) preconditioning of PS sphere suspension (via ultrasonication and preheating), (2) constant dipping and withdrawal speed, (3) coating time, and coating temperature. The AFM image of the resulting opal template is shown in Figure 2c.

The second step involves the infiltration of the metal-doped (Nd- or Nb- or co-doped) solution onto the opal template, followed by a heat treatment resulting in the formation of a hexagonally interconnected IO metal-doped SnO_2 structure (Figure 2a,d). The observed diameter of the IO template (both from FESEM and AFM images ∼ approximately 300 nm) is smaller than the original size of PS spheres, which can be explained by the shrinkage of the IO structure in the calcination steps. The resulting regular and porous IO structure would ease the insertion or extraction of Li^+ ions during the reversible electrochemical reaction.

The final step of the preparation of Nd−Nb co-doped SnO_2/α-WO_3 EC structure was the deposition of the α-WO_3 layer onto the existing IO template. Based on our previous observation, the shrinkage of pore diameter may occur during the prolonged electrodeposition of the α-WO_3 layer.[49] Figure 2b,e shows that the electrodeposition parameters used (−0.7 V for 180 s) were optimum to preserve the integrity of the porous structure. The inset of Figure 2b shows that the thickness of the resulting Nd−Nb co-doped SnO_2/α-WO_3 EC layer was approximately 1.5 μm. The representative TEM image of the "scrapped off" Nd−Nb co-doped SnO_2/α-WO_3 EC layer (sample N7) is shown in Figure 2f. The inset of Figure 2f shows the apparent crystal with the uniform lattice spacing of 0.33 nm corresponding to the (110) plane of SnO_2. The electrodeposited α-WO_3 layer was amorphous in nature because no crystalline planes of α-WO_3 layer were observed from the TEM images.

The XRD spectra of metal-doped SnO_2 IO samples are shown in Figure 3a. The crystalline SnO_2 layer was successfully infiltrated onto the opal template forming a regular IO structure. The characteristic diffraction peaks of SnO_2 (ICDD 01-070-4177) were observed in all IO samples. The peaks were located at 2θ = 22.6, 33.9, 38.0, 39.0, 42.7, 51.8, 61.9, 66.0, and 78.8°, which corresponded to the SnO_2 (110), (101), (200), (111), (210), (211), (310), (301), and (321) planes, respectively. No formation of $M_xSn_{1-x}O_2$ (M = Nb or Nd) was observed in the XRD spectra. The XRD spectra of Nd−Nb co-doped SnO_2/α-WO_3 are presented in Figure 3b. Due to the amorphous nature of the α-WO_3 layer, no crystalline α-WO_3 peaks were observed from the XRD spectra. This observation agreed with the result obtained previously from the TEM analysis.

Information of the chemical states of the ECs can be obtained through XPS analysis. The locations of all peaks were corrected against the adventitious C 1s peaks located at a binding energy of 284.8 eV. The high-resolution C 1s and O 1s XPS spectra of the representative sample N7 are shown in Figure 4a,b. The C 1s spectrum revealed that two states of

https://doi.org/10.1021/acsomega.1c03260
ACS Omega 2021, 6, 26251−26261

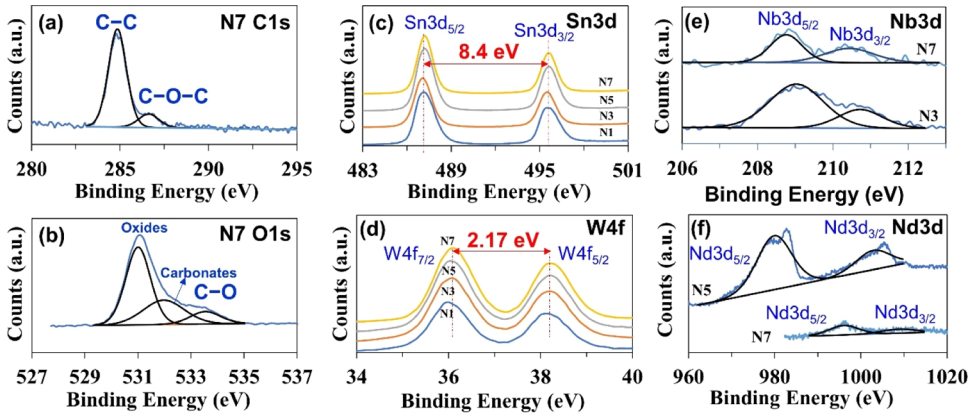

Figure 4. XPS spectra of regions (a) C 1s, (b) O 1s, (c) Sn 3d, (d) W 4f, (e) Nb 3d, and (f) Nd 3d of Nd–Nb co-doped SnO_2/α-WO_3 ECs.

chemical bonding of carbon existed within the samples, that is,, C–C (284.8 eV) and C–O–C (~286 eV). The presence of oxides, carbonates, and carbonyl C–O bonds was confirmed by the O 1s spectrum of sample N7. The symmetrical doublets of SnO_2 Sn $3d_{5/2}$ (486.6 eV) and Sn $3d_{3/2}$ (495 eV) with a peak separation of 8.4 eV that were observed for all samples indicated the presence of Sn in the chemical state of Sn^{4+} for all samples (Figure 4c). This was consistent with the results obtained from XRD analysis. Figure 4d shows the presence of symmetrical WO_3 doublets (doublet separation of 2.17 eV), indicating that W exists as W^{6+}. The high-resolution XPS spectra of Nb 3d region from the representative samples N3 and N7 are shown in Figure 4e. The Nd doublets are not well resolved due to the low concentration of Nb in the films.[26] Symmetrical Nb $3d_{3/2}$ and Nb $3d_{7/2}$ peaks suggest that majority of Nb present in the ECs are in the oxide (Nb_2O_5) form. Weak signals of Nd 3d peaks were observed for the samples that were co-doped with Nd (Figure 4f). N5 only has Nd as a dopant, while N7 has Nd and Nb as co-dopants. As such, the lower intensity of Nd 3d peaks of sample N7 was caused by a smaller fractional amount of Nd (due to the presence of the co-dopant Nb) in the sample N7 as compared to sample N5.

3.2. Stability and Switching Performance of Nd–Nb Co-doped SnO_2/α-WO_3 ECs. The spectroelectrochemical characteristics of the ECs were characterized using UV–vis–NIR spectrophotometry. The spectroelectrochemical property characterization was done under the application of +0.8 and −0.5 V bias for bleached and colored phases, respectively. Figure 5a summarizes the visible light transmittance of the EC samples measured at wavelengths of 400, 500, and 600 nm. Visible light transmission of all samples in the bleached (transparent) phase was up to 90%. The Nd–Nb co-doped samples (samples N6–N8) exhibited a high visible transmission of up to 69% (measured at 400 nm) even at the colored phase. These observations confirmed the suitability of the as-prepared samples to be used as a smart window material.

The NIR modulation capability of the samples was evaluated using the same setup as the visible light transmission. The results are summarized in Figure 5b. The value of ΔT represents the difference in % transmission between the colored and bleached phases at NIR wavelengths of interest (800, 1000, and 1200 nm). The ΔT value measured the NIR modulation, an important parameter of smart window materials. Materials with a higher NIR modulation would exhibit better smart window performance during their

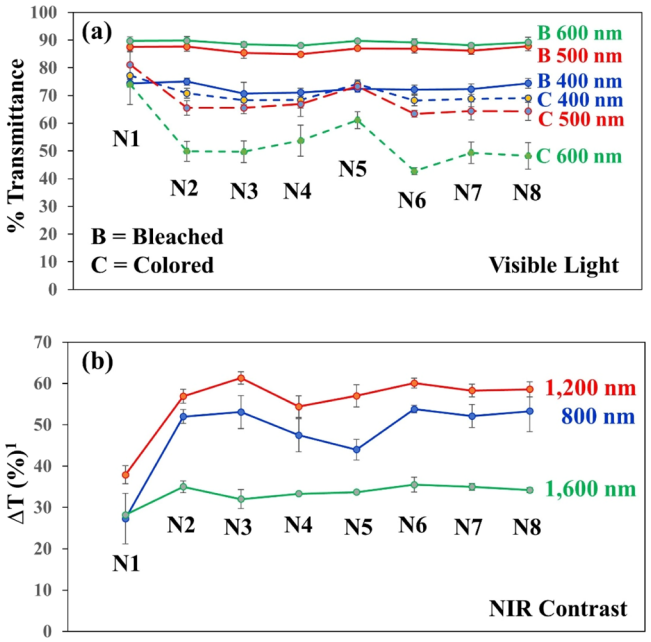

Figure 5. (a) Visible light transmittance and (b) NIR contrast of Nd–Nb co-doped SnO_2/α-WO_3 ECs ([1]difference of % transmittance at the given NIR wavelength).

application. The doped samples exhibited a much higher NIR modulation as compared to the undoped sample (N1). The NIR modulation measured at 1600 nm was relatively similar [with only a maximum 7.3% increase in NIR modulation from 28.2% (sample N1) to 35.5% (sample N6)], caused by the low penetration power of NIR radiation at 1600 nm. The enhancement of NIR modulation was observed from the samples co-doped by Nd and Nb. Sample N6 (co-doped with 5% Nb and 10% Nd) exhibited a maximum NIR modulation of 53.8, 60.1, and 35.5% measured at 800, 1200, and 1600 nm, respectively. The observed NIR modulation was almost two times of those exhibited by the undoped sample.

The UV–vis–NIR spectra of the ECs are shown in Figure 6 with the average value of the NIR contrast between the bleached and colored states measured at λ = 1033 nm embedded within. Figure 6a shows a contrasted view of the UV–vis–NIR spectra of the undoped sample (N1) versus Nd–Nb co-doped samples (N7). The overall modulation at the NIR range was widened upon the addition of Nb–Nd co-dopants. For sample N7 in the colored phase, up to 90% of

https://doi.org/10.1021/acsomega.1c03260
ACS Omega 2021, 6, 26251–26261

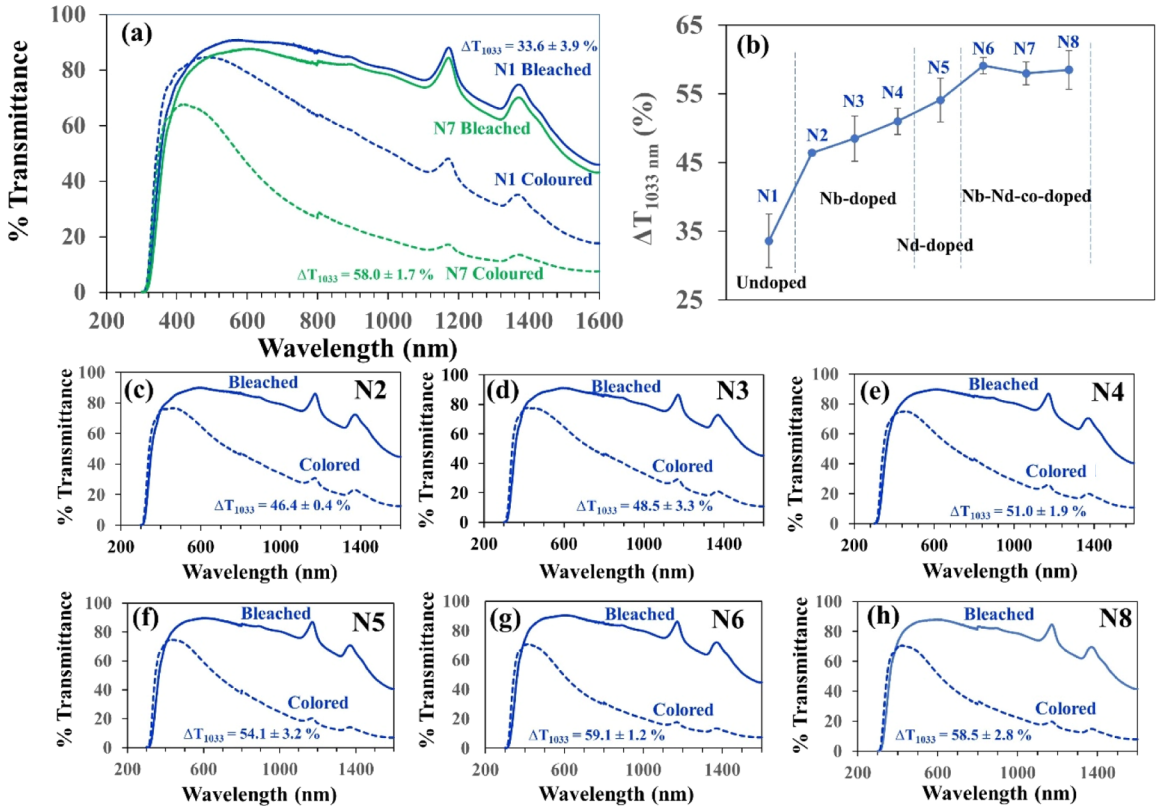

Figure 6. UV−vis−NIR spectra of Nd−Nb co-doped SnO_2/α-WO_3 ECs (a,c,d,e,f,g, and h for samples N1, N7, N2, N3, N4, N5, N6, and N8, respectively) and (b) % T measured at wavelength 1033 nm.

NIR radiation was blocked without affecting the visible light transmission (about 70% visible light transmission was still observed). On the other hand, sample N7 exhibited up to 90% of visible light and 80% of NIR heat radiation transmission when biased in the bleached state. Similar trend was observed for the other EC samples (Figure 5c−h). Figure 6b summarizes the observations of ΔT measured at wavelength = 1033 nm for all ECs. Co-doped samples exhibited a higher NIR modulation (~60%) when compared to the undoped sample (~34% of sample N1). The dual-band modulation exhibited by the Nd−Nb co-doped samples is superior as compared to the undoped sample, making them suitable candidates for smart window applications.

Another essential parameter of a good EC material is its CE. CE measured the changes in optical density caused by the insertion of electrical charge and is calculated based on eq 2. The CE values (as summarized in Figure 7) were obtained from the initial slope of the CE curves. The efficacy of Nb as a dopant material for SnO_2/α-WO_3 EC materials was evident from the up to fourfold increase of CE values for the Nb-doped samples (~496 $cm^2\ C^{-1}$ for sample N3 vs ~121 $cm^2\ C^{-1}$ for the undoped sample N1). The addition of Nd to the undoped sample also improved the CE value of the materials, although not as high as the samples doped with Nb—this observation highlights the importance of Nb as the main dopant of the system. When combined, a maximum value of CE was exhibited by sample N7 (~505 $cm^2\ C^{-1}$), which was more superior than the other reported data.[42,56,57,66] The much higher CE value highlighted the importance of co-dopants in improving the electronic conductivity of the base SnO_2/α-WO_3 EC materials.[26]

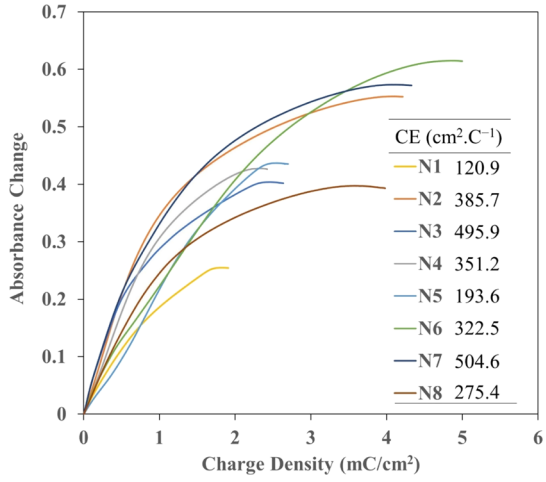

Figure 7. CE of Nd−Nb co-doped SnO_2/α-WO_3 ECs.

CV performance was measured to further understand the switching behavior of the samples. The CV plots are shown in Figure 8. The enclosed area of the CV curve represents the number of charges inserted or extracted from the ECs when an external bias was applied. Good EC materials exhibited a large CV hysteresis loop area and a high absolute peak current. Figure 8a shows the CV curves for sample N1 (undoped), N3 (Nb-doped), N5 (Nd-doped), and N7 (Nd−Nb co-doped) ECs. The area enclosed by sample N5 is slightly larger than that by sample N1, indicating that Nd doping alone may not enhance the EC properties of the sample significantly. Sample N3 doped with only Nb showed a significant increase in the area enclosed by the CV curve. This again showed the

https://doi.org/10.1021/acsomega.1c03260
ACS Omega 2021, 6, 26251−26261

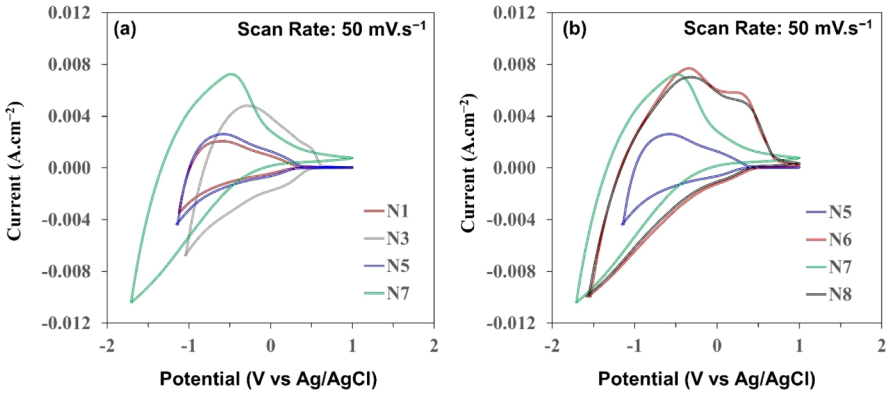

Figure 8. CV curves of Nd−Nb co-doped SnO_2/α-WO_3 ECs: (a) samples N1, N3, N5, and N7 and (b) samples N5−N8.

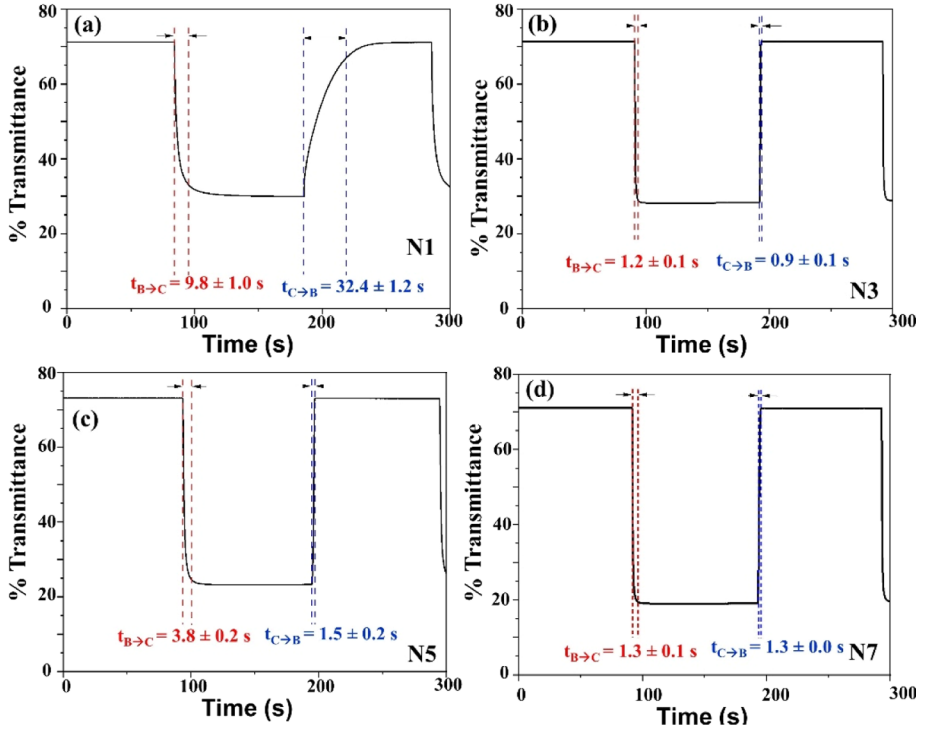

Figure 9. Switching time calculation of Nd−Nb co-doped SnO_2/α-WO_3 ECs: (a) N1, (b) N3, (c) N5, and (d) N7.

significance of Nb as the main dopant (consistent with the results obtained from CE). However, maximum enclosed CV curve area was achieved when Nd and Nb were co-doped into the ECs. The CV curves of samples N6−N8 are plotted in Figure 8b. All samples that were co-doped with Nd and Nb showed almost similar profiles of CV hysteresis curves. The difference in the shapes of the CV curves between the undoped and co-doped samples may be due to the reduced crystallinity caused by the co-dopants.[67,68] The additional oxidative peak observed only in samples N6 and N8 suggests the presence of an intermediate oxidative state. A maximum cathodic current density (~8 mA cm^{-2}) was also observed from sample N7. The reported value of peak current density was superior as compared to our previous work on Nd−Mo co-doped ECs and other published data.[57,69−71]

Fast switching times, both (bleached → colored) and (colored → bleached), are also the important aspects of good EC materials. Figure 9 illustrates the calculation of switching time (to reach 90% modulation) for the selected samples N1, N3, N5, and N7. The switching time for all samples is calculated and tabulated in Table 2. In general, the switching time from the colored to the bleached phase was shorter, except for sample N1. In terms of switching time, the effectiveness of Nb as a dopant was superior as compared to

Table 2. Switching Time and Stability of Nd−Nb Co-doped SnO_2/α-WO_3 ECs

	switching time		stability		
samples	$t_{B\to C}$ (s)	$t_{C\to B}$ (s)	$\Delta T_{initial}$	ΔT_{after}	EPD (%)
N1	9.8 ± 1.0	32.4 ± 1.2	25.7	10.6	58.7
N2	1.0 ± 0.1	1.0 ± 0.1	47.6	11.8	75.3
N3	1.2 ± 0.1	0.9 ± 0.1	39.9	7.4	81.5
N4	1.9 ± 0.1	1.5 ± 0.1	42.0	11.6	72.3
N5	3.8 ± 0.2	1.5 ± 0.2	42.5	19.5	54.1
N6	2.9 ± 0.4	1.1 ± 0.0	52.4	31.9	39.1
N7	1.3 ± 0.1	1.3 ± 0.0	42.1	27.4	35.0
N8	1.4 ± 0.1	1.6 ± 0.1	51.5	25.4	50.8

https://doi.org/10.1021/acsomega.1c03260
ACS Omega 2021, 6, 26251−26261

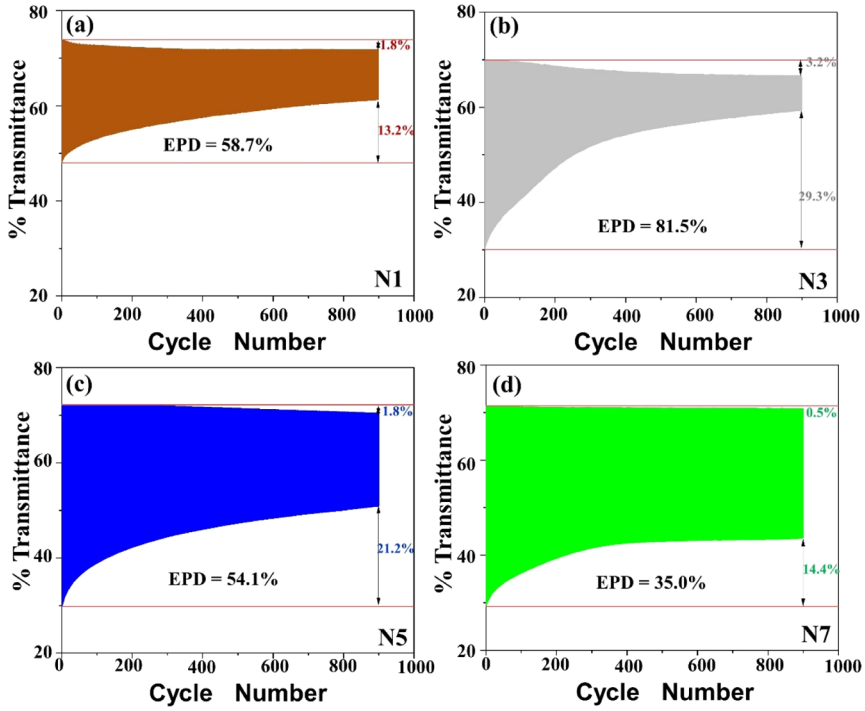

Figure 10. Stability performance of Nd−Nb co-doped SnO_2/α-WO_3 ECs: (a) N1, (b) N3, (c) N5, and (d) N7.

Nd. When N and Nb were co-doped, the overall switching time was very short (in the order of 1s), a much improved characteristic when compared with other published data.[56,72−74]

Finally, the stability of the ECs was evaluated. The samples were subjected to the reversible electrochemical cyclic test. For each cycle, the samples were subjected to 100 s of bleached phase by applying +0.8 V positive bias, followed by 100 s of colored phase by applying −0.5 V negative bias. The stability test results are presented in Figure 10. Despite a good initial NIR contrast, the sample doped only with Nb (Figure 10b) lost majority of its modulation capability—a major drawback of Nb as a dopant material. The sample doped only with Nd (Figure 10c) preserved a higher percentage of the NIR contrast. When combined, Nd and Nb synergistically improved the stability of the resulting ECs (Figure 10d). The EPD was calculated based on eq 3 and presented in the right-hand panel of Table 2. As discussed, samples doped with only Nb suffered a high percentage loss of the NIR contrast and hence showed poorer EC performance in the prolonged utilization. However, when Nd and Nb were co-doped, the overall stability improved. More than 65% of the initial NIR contrast was retained even after repeated testing cycles (sample N7). Good cyclic stability indicated the efficient intercalation and de-intercalation of charges during bleaching and coloration, resulting in a better EC performance.

The synergistic role of Nd and Nb in improving the EC properties of the resulting ECs could be ascribed to two phenomena: (a) reduced crystallization of the α-WO_3 layer and (b) minimized Li^+ trapping within the samples. Figure 11a exhibits the XRD spectra obtained from samples after the stability cycling test. New peaks corresponding to the (110) and (001) planes of the crystalline WO_3 phase (ICDD 01-073-6498) were observed at 2θ = 22.6 and 23.7°. The peaks were not observed in other samples, indicating the reduced crystallization of the α-WO_3 layer on the doped samples.[49,50]

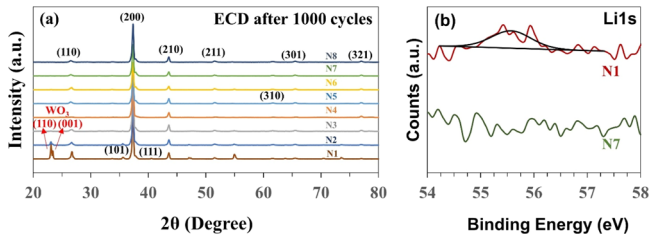

Figure 11. (a) XRD spectra of Nd−Nb co-doped SnO_2/α-WO_3 ECs after the stability cycling test and (b) high-resolution XPS spectra showing the Li 1s region of samples N1 and N7 after the stability cycling test.

Further evidence on the role of Nd and Nb co-dopants that synergistically improved the EC performance of the SnO_2/α-WO_3 ECs is explained in Figure 11b. The presence of Li 1s peaks on the post-stability test sample N1 suggested the entrapment of Li^+. No Li^+ ions were observed for other doped samples. The electronic conductivity of the co-doped samples was enhanced by the excess electrons transferred from the Nd and Nb co-dopants to the conduction band of SnO_2. The improved electronic conductivity of SnO_2/α-WO_3 ECs was achieved by the increased free charge carriers donated by metal ion dopants to the host lattice and improved electron mobility caused by the formation of electron-transfer channels within the EC framework.[40,58,59]

The Nd−Nb co-doped SnO_2/α-WO_3 ECs could also be systemically coated on a larger FTO template. An upscaled device consisting of 100 × 100 mm^2 of EC material-coated FTO can be prepared (Figure 1). The upscaled ECs exhibited a very similar EC characteristic as that of the smaller samples used in this study. The combination of both superior visible light transparency and high NIR contrast, rapid switching time, and excellent stability justified the choice of Nd−Nb co-doped SnO_2/α-WO_3 ECs as outstanding smart window materials.

https://doi.org/10.1021/acsomega.1c03260
ACS Omega 2021, 6, 26251−26261

4. CONCLUSIONS

The design and fabrication of novel Nd−Nb co-doped SnO_2/α-WO_3 ECs are presented. The morphology and physicochemical properties of the materials were characterized, and the optical and electrochemical performances of the materials were evaluated. The enhancement of electrochemical performances caused by the synergistic actions of the added co-dopants (Nd and Nb) was investigated. The co-dopants would transfer their excess electrons to SnO_2, improving the electronic conductivity of the ECs and easing the insertion and extraction of Li^+ cations into the structure. The presence of co-dopants also was found to reduce the crystallization rate of the α-WO_3 phase. Sample N7 (samples doped by 10% Nd and 10% Nb) exhibited 90% visible light transmission, 60% NIR contrast, high coloration efficiency (~505 cm^2 C^{-1}), fast switching time (~1 s), and small EPD (~35% after 1000× repeated stability test cycles). The novel combination of Nd−Nb co-doped SnO_2/α-WO_3 presented in this work is an excellent candidate material for smart window application to be used in green buildings. Beyond this, it showed the potential to be used for electronic displays, electronic papers, eyewear, automotive smart windows, and many other applications.

AUTHOR INFORMATION

Corresponding Authors

Ronn Goei − *School of Materials Science and Engineering, Nanyang Technological University, Singapore 639798, Singapore; Singapore-HUJ Alliance for Research and Enterprise, Singapore 138602, Singapore;* Email: Ronn_goei@ntu.edu.sg

Alfred Iing Yoong Tok − *School of Materials Science and Engineering, Nanyang Technological University, Singapore 639798, Singapore; Singapore-HUJ Alliance for Research and Enterprise, Singapore 138602, Singapore;* orcid.org/0000-0003-3546-7180; Email: miytok@ntu.edu.sg

Authors

Amanda Jiamin Ong − *School of Materials Science and Engineering, Nanyang Technological University, Singapore 639798, Singapore; Singapore-HUJ Alliance for Research and Enterprise, Singapore 138602, Singapore*

Jun Hao Tan − *School of Materials Science and Engineering, Nanyang Technological University, Singapore 639798, Singapore*

Jie Yi Loke − *School of Materials Science and Engineering, Nanyang Technological University, Singapore 639798, Singapore*

Shun Kuang Lua − *School of Materials Science and Engineering, Nanyang Technological University, Singapore 639798, Singapore*

Daniel Mandler − *Singapore-HUJ Alliance for Research and Enterprise, Singapore 138602, Singapore; Institute of Chemistry, The Hebrew University of Jerusalem, Jerusalem 9190401, Israel;* orcid.org/0000-0003-2490-1084

Shlomo Magdassi − *Singapore-HUJ Alliance for Research and Enterprise, Singapore 138602, Singapore; Institute of Chemistry, The Hebrew University of Jerusalem, Jerusalem 9190401, Israel;* orcid.org/0000-0002-6794-0553

Complete contact information is available at: https://pubs.acs.org/10.1021/acsomega.1c03260

Notes

The authors declare no competing financial interest.

ACKNOWLEDGMENTS

This research was supported by grants from the National Research Foundation, Prime Minister's Office, Singapore, under its Campus of Research Excellence and Technological Enterprise (CREATE) Program.

REFERENCES

(1) Research and Statistics Unit, E.M.A.S *Singapore Energy Statistics 2019*; Energy Market Authority Singapore: Singapore, 2020.

(2) Singapore, D.o.S *Singapore Population*, 2020. cited 2020 3 November 2020].

(3) Agency, I. E. *World Energy Balance: Overview*; International Energy Agency: Paris, 2020.

(4) Llordés, A.; et al. Tunable near-infrared and visible-light transmittance in nanocrystal-in-glass composites. *Nature* **2013**, *500*, 323−326.

(5) Granqvist, C. G. Electrochromics for smart windows: Oxide-based thin films and devices. *Thin Solid Films* **2014**, *564*, 1−38.

(6) Platt, J. R. Electrochromism, a Possible Change of Color Producible in Dyes by an Electric Field. *J. Chem. Phys.* **1961**, *34*, 862−863.

(7) Macrelli, G. Electrochromic Windows. *World Renewable Energy Congress VI*; Sayigh, A. A. M., Ed.; Pergamon: Oxford, 2000; Chapter 35, p 177−183.

(8) Wang, Y.; Runnerstrom, E. L.; Milliron, D. J. Switchable Materials for Smart Windows. *Annu. Rev. Chem. Biomol. Eng.* **2016**, *7*, 283−304.

(9) Wu, L.; et al. A multifunctional smart window: Detecting ultraviolet radiation and regulating the spectrum automatically. *J. Mater. Chem. C* **2019**, *7*, 10446−10453.

(10) Beaujuge, P. M.; Ellinger, S.; Reynolds, J. R. The donor−acceptor approach allows a black-to-transmissive switching polymeric electrochrome. *Nat. Mater.* **2008**, *7*, 795−799.

(11) Lang, A. W.; et al. Transparent Wood Smart Windows: Polymer Electrochromic Devices Based on Poly(3,4-Ethylenedioxythiophene):Poly(Styrene Sulfonate) Electrodes. *ChemSusChem* **2018**, *11*, 854−863.

(12) Lang, F. P.; et al. Review on Variable Emissivity Materials and Devices Based on Smart Chromism. *Int. J. Thermophys.* **2018**, *39*, 6.

(13) Lv, X.; et al. An all-solid-state polymeric electrochromic device based on two well-matched electrodes with fast switching time and excellent cycling stability. *React. Funct. Polym.* **2020**, *156*, 104737.

(14) Yemata, T. A.; et al. Modulation of the doping level of PEDOT:PSS film by treatment with hydrazine to improve the Seebeck coefficient. *RSC Adv.* **2020**, *10*, 1786−1792.

(15) Ito, S.; et al. Electrochromic properties of iridium oxide thin films prepared by reactive sputtering in O_2 or H_2O atmosphere. *J. Vac. Sci. Technol., B: Nanotechnol. Microelectron.: Mater., Process., Meas., Phenom.* **2015**, *33*, 041204.

(16) Wen, R.-T.; Niklasson, G. A.; Granqvist, C. G. Electrochromic iridium oxide films: Compatibility with propionic acid, potassium hydroxide, and lithium perchlorate in propylene carbonate. *Sol. Energy Mater. Sol. Cells* **2014**, *120*, 151−156.

(17) Wen, R.-T.; Niklasson, G. A.; Granqvist, C. G. Electrochromic iridium-containing nickel oxide films with excellent electrochemical cycling performance. *J. Electrochem. Soc.* **2016**, *163*, E7−E13.

(18) Arash, A.; et al. Electrically Activated UV-A Filters Based on Electrochromic MoO_{3-x}. *ACS Appl. Mater. Interfaces* **2020**, *12*, 16997−17003.

(19) Chang, C.-C.; et al. Electrochemistry and rapid electrochromism control of MoO_3/V_2O_5 hybrid nanobilayers. *Materials* **2019**, *12*, 2475.

(20) Kumar, A.; Prajapati, C. S.; Sahay, P. P. Results on the microstructural, optical and electrochromic properties of spray-

deposited MoO_3 thin films by the influence of W doping. *Mater. Sci. Semicond. Process.* **2019**, *104*, 104668.
(21) Lee, C.-T.; et al. Synthesis and electrochromic properties of molybdenum oxide films. *Surf. Coat. Technol.* **2019**, *363*, 426−429.
(22) Firat, Y. E.; Peksoz, A. Efficiency enhancement of electrochromic performance in NiO thin film via Cu doping for energy-saving potential. *Electrochim. Acta* **2019**, *295*, 645−654.
(23) Pan, J.; et al. A high-performance electrochromic device assembled with hexagonal WO_3 and NiO/PB composite nanosheet electrodes towards energy storage smart window. *Sol. Energy Mater. Sol. Cells* **2020**, *207*, 110337.
(24) Rakibuddin, M.; Shinde, M. A.; Kim, H. Sol-gel fabrication of NiO and NiO/WO_3 based electrochromic device on ITO and flexible substrate. *Ceram. Int.* **2020**, *46*, 8631−8639.
(25) Wang, K.-H.; et al. Nanometer-Thick Nickel Oxide Films Prepared from Alanine-Chelated Coordination Complexes for Electrochromic Smart Windows. *ACS Appl. Nano Mater.* **2020**, *3*, 9528−9537.
(26) Bathe, S. R.; Patil, P. S. Influence of Nb doping on the electrochromic properties of WO_3 films. *J. Phys. D: Appl. Phys.* **2007**, *40*, 7423−7431.
(27) Bueno, P. R.; Gabrielli, C.; Perrot, H. Coloring ionic trapping states in WO_3 and Nb_2O_5 electrochromic materials. *Electrochim. Acta* **2008**, *53*, 5533−5539.
(28) Mjejri, I.; Grocassan, R.; Rougier, A. Enhanced Coloration for Hybrid Niobium-Based Electrochromic Devices. *ACS Appl. Energy Mater.* **2018**, *1*, 4359−4366.
(29) Tian, Z.; et al. Enhanced Charge Injection and Collection of Niobium-Doped TiO_2/Gradient Tungsten-Doped $BiVO_4$ Nanowires for Efficient Solar Water Splitting. *ACS Appl. Energy Mater.* **2018**, *1*, 1218−1225.
(30) Wang, C.-K.; et al. Electrochromic Nb-doped WO_3 films: Effects of post annealing. *Ceram. Int.* **2012**, *38*, 2829−2833.
(31) Cao, S.; et al. Fluoride-Assisted Synthesis of Plasmonic Colloidal Ta-Doped TiO_2 Nanocrystals for Near-Infrared and Visible-Light Selective Electrochromic Modulation. *Chem. Mater.* **2018**, *30*, 4838−4846.
(32) Dhandayuthapani, T.; et al. Brown coloration and electrochromic properties of nickel doped TiO_2 thin films deposited by nebulized spray pyrolysis technique. *Thin Solid Films* **2020**, *694*, 137754.
(33) Ling, H.; et al. TiO_2-WO_3 core-shell inverse opal structure with enhanced electrochromic performance in NIR region. *J. Mater. Chem. C* **2018**, *6*, 8488−8494.
(34) Zhang, S.; et al. Plasmonic Oxygen-Deficient TiO_{2-x} Nanocrystals for Dual-Band Electrochromic Smart Windows with Efficient Energy Recycling. *Adv. Mater.* **2020**, *32*, 2004686.
(35) Cai, G.; et al. Ultra-large optical modulation of electrochromic porous WO3 film and the local monitoring of redox activity. *Chem. Sci.* **2016**, *7*, 1373−1382.
(36) de León, J. M. O.-R.; et al. Improving electrochromic behavior of spray pyrolised WO_3 thin solid films by Mo doping. *Electrochim. Acta* **2011**, *56*, 2599−2605.
(37) Deb, S. K. Opportunities and challenges in science and technology of WO_3 for electrochromic and related applications. *Sol. Energy Mater. Sol. Cells* **2008**, *92*, 245−258.
(38) Hashimoto, S.; Matsuoka, H. Mechanism of electrochromism for amorphous WO_3 thin films. *J. Appl. Phys.* **1991**, *69*, 933−937.
(39) Kavitha, V. S.; et al. Tb^{3+}-doped WO_3 thin films: A potential candidate in white light emitting devices. *J. Alloys Compd.* **2019**, *788*, 429−445.
(40) Nah, Y.-C.; et al. TiO_2−WO_3 Composite Nanotubes by Alloy Anodization: Growth and Enhanced Electrochromic Properties. *J. Am. Chem. Soc.* **2008**, *130*, 16154−16155.
(41) Pehlivan, E.; Tepehan, F. Z.; Tepehan, G. G. Comparison of optical, structural and electrochromic properties of undoped and WO_3-doped Nb_2O_5 thin films. *Solid State Ionics* **2003**, *165*, 105−110.
(42) Yang, H.; et al. Enhanced electrochromic properties of nanorod based WO_3 thin films with inverse opal structure. *Thin Solid Films* **2018**, *660*, 596−600.
(43) Hao, R. L.; et al. Optical modulation characteristics of VO_2 thin film due to electric field induced phase transition in the FTO/VO_2/FTO structure. *Acta Phys. Sin* **2015**, *64*, 198101.
(44) Lee, S. J.; et al. VO_2/WO_3-Based Hybrid Smart Windows with Thermochromic and Electrochromic Properties. *ACS Sustainable Chem. Eng.* **2019**, *7*, 7111−7117.
(45) Mjejri, I.; Gaudon, M.; Rougier, A. Mo addition for improved electrochromic properties of V_2O_5 thick films. *Sol. Energy Mater. Sol. Cells* **2019**, *198*, 19−25.
(46) Zhang, X.; et al. Inorganic all-solid-state electrochromic devices with reversible color change between yellow-green and emerald green. *Chem. Commun.* **2020**, *56*, 10062−10065.
(47) Chatzikyriakou, D.; et al. Mesoporous amorphous tungsten oxide electrochromic films: a Raman analysis of their good switching behavior. *Electrochim. Acta* **2014**, *137*, 75−82.
(48) Randin, J. P. Chemical and electrochemical stability of WO_3 electrochromic films in liquid electrolytes. *J. Electron. Mater.* **1978**, *7*, 47−63.
(49) Nguyen, T. D.; et al. Efficient Near Infrared Modulation with High Visible Transparency Using SnO_2 −WO_3 Nanostructure for Advanced Smart Windows. *Adv. Opt. Mater.* **2019**, *7*, 1970031.
(50) Arvizu, M. A.; et al. Electrochromism in sputter-deposited W−Ti oxide films: Durability enhancement due to Ti. *Sol. Energy Mater. Sol. Cells* **2014**, *125*, 184−189.
(51) Wen, R.-T.; Granqvist, C. G.; Niklasson, G. A. Eliminating degradation and uncovering ion-trapping dynamics in electrochromic WO_3 thin films. *Nat. Mater.* **2015**, *14*, 996−1001.
(52) Zhang, J.; et al. Enhanced electrochromic performance of highly ordered, macroporous WO_3 arrays electrodeposited using polystyrene colloidal crystals as template. *Electrochim. Acta* **2013**, *99*, 1−8.
(53) Zhang, X.; et al. Preparation of monolayer hollow spherical tungsten oxide films with enhanced near infrared electrochromic performances. *Electrochim. Acta* **2019**, *297*, 223−229.
(54) Kuroki, T.; Matsushima, Y.; Unuma, H. Electrochromic response of WO_3 and WO_3-TiO_2 thin films prepared from water-soluble precursors and a block copolymer template. *J. Asian Ceram. Soc.* **2016**, *4*, 367−370.
(55) Hashimoto, S.; Matsuoka, H. Prolonged lifetime of electrochromism of amorphous WO_3−TiO_2 thin films. *Surf. Interface Anal.* **1992**, *19*, 464−468.
(56) Nguyen, T. D.; et al. Electrochromic smart glass coating on functional nano-frameworks for effective building energy conservation. *Mater. Today Energy* **2020**, *18*, 100496.
(57) Goei, R.; et al. Novel Nd−Mo co-doped SnO_2/α-WO_3 electrochromic materials (ECs) for enhanced smart window performance. *Ceram. Int.* **2021**, *47*, 18433−18442.
(58) Kim, K.-H.; Koo, B.-R.; Ahn, H.-J. Effects of Sb-doped SnO_2−WO_3 nanocomposite on electrochromic performance. *Ceram. Int.* **2019**, *45*, 15990−15995.
(59) Posthumus, W.; et al. Control of the electrical conductivity of composites of antimony doped tin oxide (ATO) nanoparticles and acrylate by grafting of 3-methacryloxypropyltrimethoxysilane (MPS). *J. Colloid Interface Sci.* **2006**, *304*, 394−401.
(60) Reichman, B.; Bard, A. J. Electrochromism at Niobium Pentoxide Electrodes in Aqueous and Acetonitrile Solutions. *J. Electrochem. Soc.* **1980**, *127*, 241−242.
(61) Wang, W. Q.; et al. Niobium doped tungsten oxide mesoporous film with enhanced electrochromic and electrochemical energy storage properties. *J. Colloid Interface Sci.* **2019**, *535*, 300−307.
(62) Yu, C.; et al. Solvothermal growth of Nb_2O_5 films on FTO coated glasses and their electrochromic properties. *Ceram. Int.* **2021**, *47*, 9651−9658.
(63) Kabtamu, D. M.; et al. Electrocatalytic activity of Nb-doped hexagonal WO_3 nanowire-modified graphite felt as a positive electrode for vanadium redox flow batteries. *J. Mater. Chem. A* **2016**, *4*, 11472−11480.

https://doi.org/10.1021/acsomega.1c03260
ACS Omega 2021, 6, 26251−26261

(64) Zheng, L.; Shah, K. W. Electrochromic Smart Windows for Green Building Applications. *Electrochromic Smart Materials: Fabrication and Applications*; The Royal Society of Chemistry, 2019; Chapter 16, pp 494−520.
(65) Nguyen, T. D.; et al. Electrodeposition of amorphous WO_3 on SnO_2-TiO_2 inverse opal nano-framework for highly transparent, effective and stable electrochromic smart window. *RSC Adv.* **2019**, *9*, 16730−16737.
(66) Chen, Y.; et al. High-Coloration Efficiency Electrochromic Device Based on Novel Porous TiO_2@Prussian Blue Core-Shell Nanostructures. *Electrochim. Acta* **2017**, *224*, 534−540.
(67) Brezesinski, T.; et al. Highly Crystalline WO_3 Thin Films with Ordered 3D Mesoporosity and Improved Electrochromic Performance. *Small* **2006**, *2*, 1203−1211.
(68) Cai, G.-f.; et al. Hierarchical structure Ti-doped WO_3 film with improved electrochromism in visible-infrared region. *RSC Adv.* **2013**, *3*, 6896−6905.
(69) Deepa, M.; et al. Nanostructured mesoporous tungsten oxide films with fast kinetics for electrochromic smart windows. *Nanotechnology* **2006**, *17*, 2625−2630.
(70) More, A. J.; et al. Electrodeposition of nano-granular tungsten oxide thin films for smart window application. *Mater. Lett.* **2014**, *134*, 298−301.
(71) More, A. J.; et al. Synthesis and Characterization of Potentiostatically Electrodeposited Tungsten Oxide Thin Films for Smart Window Application. *J. Electron. Mater.* **2017**, *46*, 974−981.
(72) Wang, J.; et al. Controlled Synthesis of WO_3 Nanorods and Their Electrochromic Properties in H_2SO_4 Electrolyte. *J. Phys. Chem. C* **2009**, *113*, 9655−9658.
(73) Wang, X.; et al. Mo-doped SnO_2 mesoporous hollow structured spheres as anode materials for high-performance lithium ion batteries. *Nanoscale* **2015**, *7*, 3604−3613.
(74) Zhou, B.; et al. A low cost preparation of WO_3 nanospheres film with improved thermal stability of gasochromic and its application in smart windows. *Mater. Res. Express* **2017**, *4*, 115702.

https://doi.org/10.1021/acsomega.1c03260
ACS Omega 2021, 6, 26251−26261